Interaction and Multiscale Mechanics, *Vol.6, No.2 (2013) 257-270*
DOI: http://dx.doi.org/10.12989/imm.2013.6.2.257

A coupled finite element/meshfreemoving boundary method for self-piercing riveting simulation

Wayne Cai*[1], Hui-Ping Wang[1] and C.T. Wu[2]

[1]*Research and Development Center, General Motors R&D Center, 30500 Mound Road, Warren, MI 48090, USA*
[2]*Livermore Software Technology Corporation, 7374 Las Positas Road, Livermore, CA 94550, USA*

(Received March 1, 2013, Revised April 23, 2013, Accepted May 6, 2013)

Abstract. The use of lightweight materials has been steadily increasing in the automotive industry, and presents new challenges to material joining. Among many joining processes, self-piercing riveting (SPR) is particularly promising for joining lightweight materials (such as aluminum alloys) and dissimilar materials (such as steel to Al, and metal to polymer). However, to establish a process window for optimal joint performance, it often requires a long trial-and-error testing of the SPR process. This is because current state of the art in numerical analysis still cannot effectively resolve the problems of severe material distortion and separation in the SPR simulation. This paper presents a coupled meshfree/finite element with a moving boundary algorithm to overcome these numerical difficulties. The simulation results are compared with physical measurements to demonstrate the effectiveness of the present method.

Keywords: meshfree method; element free galerkinmethod; finite element method; moving boundary; self piercingriveting

1.Introduction

Today's vehicle manufacture heavily relies on computer-aided engineering (CAE) analysis. In most scenarios, the CAE analysis provides a quick and cost-effective assessment of the manufacturing process feasibility. Also, the analysis helps improve the design by virtually optimizing process parameters to achieve the design target. With the help of the CAE analysis, the amount of expensive and time-consuming physical tests is greatly reduced. Still, there are scenarios that current CAE technologies cannot comprehend well. Exemplary problems are events and processes involving severe deformation, material separation, fluid-solid interaction, phase changing and other complex physics. The self-piercing riveting (SPR) process addressed in this paper is one of these challenging problems. SPR is a high-speed cold mechanical joining process without fusion or heat input. As illustrated in Fig. 1, a semi-tubular rivet is driven into the materials to be joined between a punch and a die in a press tool. The rivet drives through the toplayers and toward the die, where the die shape causes the rivet skirt to flare within the lower layer and forms a mechanical interlock.

*Corresponding author, Ph.D.,E-mail:wanye.cai@gm.com

http://www.techno-press.org/?journal=imm&subpage=7 ISSN: 1976-0426 (Print), 2092-6200 (Online)

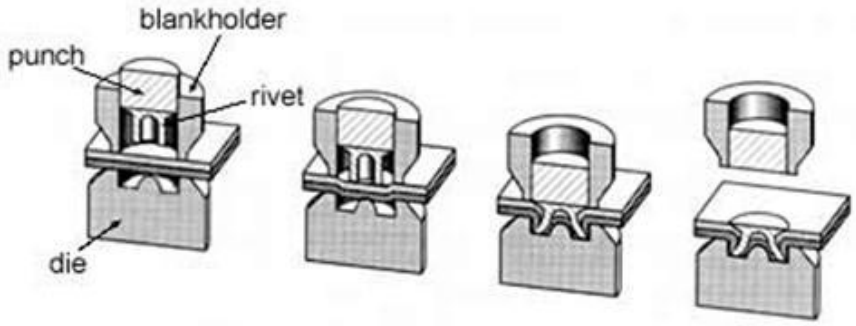

Fig. 1 A schematic representation of the self-piercing riveting process (TWI 2000)

It is particularly attractive for joining lightweight materials (such as aluminum alloys), dissimilar materials, and coated or pre-painted sheets (Sunday 1983, Hill 1994, Litherland 1998). With the increasing use of mixed lightweight materials in the automotive industry under the drive for better fuel efficiency, the SPR process is nowadays becoming more and more popular for vehicle assembly. For example, the aluminum constructed body-in-white of the Jaguar XJ uses 3200 self-piercing rivets (Jaguar 2013). However, to establish a process window for optimal SPR joint performance, it often requires time-consuming and expensive trial-and-error tests. Therefore, it is necessary to develop effective CAE analysis tools such as finite element modeling schemes to accurately and effectively simulate the SPR processes.

Many studies have been performed to develop reliable SPR numerical models and calibrate them with experimental data. The early modeling work can be traced back to King's thesis work in 1997 (King 1997), where a very basic finite element (FE) model was created to model the indentation of a SPR process. Most other modeling works were published in recent years after the finite element method has become more stable in terms of handling contact constraints, mesh distortion and crack propagation. Porcaro*et al*. (2004, 2006) modeled the process using the commercial tool LS-Dyna, where r-adaptivity was used to prevent mesh distortion and a geometric failure criterion based on the change in thickness of the connected plates was employed to trigger the adaptivity. To consider material separation in the SPR simulation, Bouchard *et al.* (2008) implemented a Lemaitre coupled damage model with 'kill-element' technique in the Forge2005® finite element software to address the damage in the process and additional 'kill-element' criterion which was based on the element quality to remove distorted elements. Cai*et al.* (2005) reported dimension analysis of riveted assembly by using mixed empirical-analytical approach, without modeling the local SPR distortion and material damage. Casalino*et al*. (2008) used LS-Dyna to model the SPR process with attention to finding the right mesh size and critical damage parameters. Sun and Khaleel (2005) studied the strength optimization and failure mode prediction of self-piercing rivets (SPRs) for automotive applications. Masters *et al.* (2012) presented a simulation method based on a local/global approach where the distortion occurring around a single SPR was projected on to a global assembly at each rivet location. An overview on the state of the art of the research on the SPR was given by He *et al*. (2012), where the latest finite element modeling approaches on the SPR process were listed. In all the above mentioned work, finite element methods with either an implicit or explicit solution techniques have been used in the SPR simulation. Research efforts inevitably focused on how to model the large material distortion and

separation accurately. The experimental data of progressive sectional profiles and curve of the piercing force versus the piercing displacement were commonly used to calibrate the numerical models.

The conventional mesh-based finite element method models the physical domain with discrete, non-overlapping and conforming meshes. The order of the finite element approximation being constructed at each element degenerates when the element has aspect-ratio or geometric distortion. Consequently, the accuracy of the finite element based CAE analysis degrades or even the analysis fails. This is especially true in the simulations of severe deformation or large shape change such as the ones in the SPR process even if adaptive remeshing is used. Meshfree methods are a series of methods proposed and developed to resolve the mesh-distortion difficulty since 1990s due to their 'meshfree' characteristics. Typical meshfree methods are Element-free Galerkin (EFG) Method, Reproducing Kernel Particle Method, HP-clouds method, Partition of Unity method (Belytschko*et al*. 1994, Liu *et al.* 1995, Chen *et al.* 1996, Melenk an Babuska 1996, Duarte and Oden 1996) and more recently the convex meshfree method (Wu *et al*. 2011). The common feature of these methods is the construction of the approximation functions at discrete points of a domain without the usage of element connectivity among the discrete points. The approximation functions are then applied in interpolating field variables so that the corresponding math models can be solved in the approximated domain. These approximation functions are naturally conforming, and can have high order smoothness and exactly approximate high order monomials; therefore, meshfree approximations can better model problems with material interface (Wu *et al*. 2013) and nonlinearity. Preliminary applications of these approximations in solving nonlinear large deformation (Chen *et al*. 1996) or material separation problems (Fleming *et al*. 1997, Krongauz and Belytschko 1998) have shown their great advantages over the conventional finite element methods in terms of model adaptivity and solution accuracy. However, the meshfree methods are generally more computational extensive than the FE methods, greatly limiting their potentials in solving large-scale industrial problems. Many versions of the coupled meshfree/finite element method (Cai*et al.* 2004, Wang *et al*. 2009, Wu *et al*. 2012) reduced the high CPU consumption of meshfree computation to local distortion zone by modeling the remaining area with the finite element method. It makes the meshfree method available for modeling large-scale industrial problems where the number of degrees of freedom (DOFs) in the distortion region is small relative to the overall number of DOFs in the model.

In this paper, a coupled meshfree/finite element method is employed in conjunction with a moving boundary algorithm to model the self-pierce riveting problem. The whole paper is organized as follows: Section 2 reviews the Moving Least-squares (MLS) approximation and the coupled meshfree/finite element method. Section 3 describes the moving boundary algorithm, material damage law and their implementations in LS-DYNA. Section 4 reports a simulation of the SPR process using the present method and with a comparison to experimental result. Conclusions are made in Section 5.

2. Overview on moving least-squares approximation (MLS) and a coupled meshfree/finite method

2.1 MLS approximation

The meshfree method employed in this research is the EFG method developed in (Belytschko

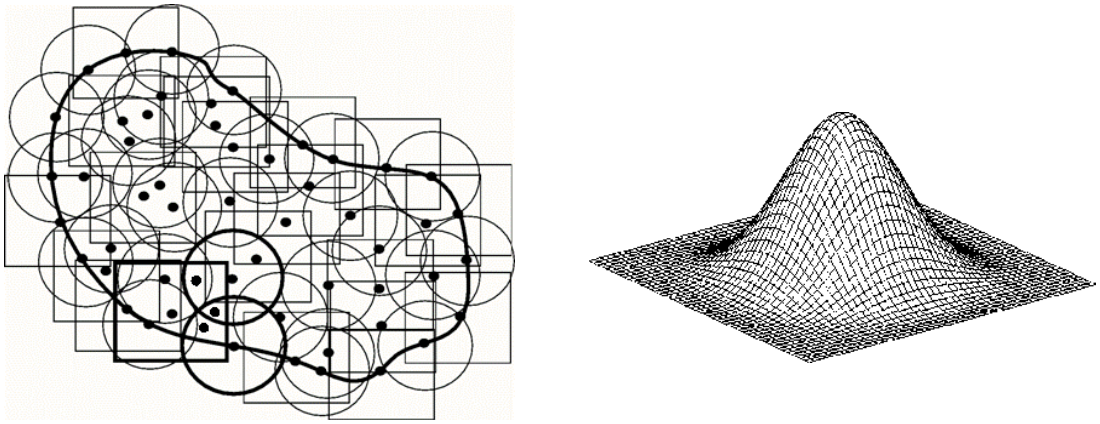

(a) Meshfree discretization (b) Meshfree shape function

Fig.1 Example of meshfree discretization and shape function in two-dimensional domain

et al. 1995). The EFG method was one of the meshless methods for the large deformation analysis. When damage appears in severe deformation, the visibility criterion introduces discontinuity and avoids any tangling of the integration cell. The Moving Least Squares (MLS) approximation is used to construct the shape function in the EFG method. Let **u** be a function defined on a domain Ω, and let the domain Ω be discretized by a set of points $\{\mathbf{x}_I\}_{I=1}^{NP} \subset \Omega$. The MLS approximation of the function **u**(**x**), denoted by $u^h(\mathbf{x})$, is

$$\mathbf{u}^h(\mathbf{x}) = \sum_{j=1}^{n} b_j h_j(\mathbf{x}) = \mathbf{h}^{[n]T}(\mathbf{x})\mathbf{b}^{[n]} \tag{1}$$

where $\mathbf{h}^{[n]}(\mathbf{x}) = \left(1, x, y, x^2, \cdots, y^n\right)^T$ is the vector of a monomial basis in the coordinates $\mathbf{x}^T = [x, y]$ in a two dimensional domain, and $\mathbf{h}^{[n]}(\mathbf{x}) = (1, x, y, z, x^2, \cdots, z^n)^T$ a vector of a monomial basis in $\mathbf{x}^T = [x, y, z]$ in a three dimensional domain so that the basis is complete. The coefficientsb_j, j = 1, 2, …,n are solved by minimizing the following weighted, discreteL_2 norm

$$E(b_j) = \sum_{I=1}^{NP} \Phi_a(\mathbf{x} - \mathbf{x}_I)\left(\sum_{j=1}^{n} b_j h_j(\mathbf{x}_I) - \mathbf{u}(\mathbf{x}_I)\right)^2 \tag{2}$$

$\Phi_a(\mathbf{x} - \mathbf{x}_I)$ is the weight function which attaches to each point and has a compact support "a". When $\partial E(b_j)/\partial b_j = 0$, the coefficients b_j are solved as

$$\mathbf{b}^{[n]}(\mathbf{x}) = \sum_{I=1}^{NP} \Phi_a(\mathbf{x} - \mathbf{x}_I)\mathbf{M}^{[n]-1}(\mathbf{x})\mathbf{h}^{[n]}(\mathbf{x}_I)\mathbf{u}(\mathbf{x}_I) \tag{3}$$

$$\mathbf{M}^{[n]}(\mathbf{x})=\sum_{J=1}^{NP}\Phi_a(\mathbf{x}-\mathbf{x}_J)\mathbf{h}^{[n]}(\mathbf{x}_J)\mathbf{h}^{[n]^T}(\mathbf{x}_J) \tag{4}$$

assuming $\mathbf{M}^{[n]}(\mathbf{x})$ is non-singular. For the case $n=1$, a sufficient condition for a non-singular $\mathbf{M}^{[1]}(\mathbf{x})$ is that $\mathbf{x}$ for $\mathbf{x}\in\Omega$ is at least covered by the supports of four weight functions $\Phi_a(\mathbf{x}-\mathbf{x}_J)$, $J=1,2,3,4$, where $\mathbf{x}_1$, $\mathbf{x}_2$, $\mathbf{x}_3$ and $\mathbf{x}_4$ are not on the same plane in the three dimensional problem. Substituting Eq. (3) into Eq. (1), the MLS interpolant can be expressed as

$$\mathbf{u}^h(\mathbf{x})=\sum_{I=1}^{NP}\Psi_I^{[n]}(\mathbf{x};\mathbf{x}-\mathbf{x}_I)\mathbf{u}(\mathbf{x}_I) \tag{5}$$

$$\Psi_I^{[n]}(\mathbf{x};\mathbf{x}-\mathbf{x}_I)=\Phi_a(\mathbf{x}-\mathbf{x}_I)\mathbf{h}^{[n]^T}(\mathbf{x})\mathbf{M}^{[n]^{-1}}(\mathbf{x})\mathbf{h}^{[n]}(\mathbf{x}_I) \tag{6}$$

where $\Psi_I^{[n]}(\mathbf{x};\mathbf{x}-\mathbf{x}_I)$ is the MLS shape function.

Fig. 2 is a two-dimensional example of a MLS shape function constructed using a cubic B-spline weight function with a linear basis. The employment of the MLS shape functions in the Galerkin approximation of a PDE is called the EFG method.

Notice that $\Psi_I^{[n]}(\mathbf{x};\mathbf{x}-\mathbf{x}_I)$ in Eq. (6) is generally not an interpolation function, that is, the MLS shape functions do not have Kronecker-delta properties and $\mathbf{u}^h(\mathbf{x}_I)$ may not be equal to $\mathbf{u}(\mathbf{x}_I)$ in Eq. (5). Because of this lack of Kronecker-delta property, special treatments are necessary when the MLS shape functions are used to approximate boundary value problems. Additional computation is needed to calculate $\mathbf{u}^h(\mathbf{x}_I)$ from the coefficients $\mathbf{u}(\mathbf{x}_I)$, *I=1,2,...,NP* using Eq. (5) compared to the finite element method. Also, the resulting stiffness matrix for the linear system of algebraic equation after these treatments is usually neither banded nor sparse. This is why the solution of the linear system in the meshfree method is computationally intensive, which is especially evident in an implicit computation.

2.2 Coupled mshfree/fniteelement method

The purpose of coupling the meshfree method and the FE method is to keep computational cost low from the meshfree modeling so that the problems can be solved efficiently.illustrates the main concept of this coupling. The problem domain Ω is divided into FE sub-domains and meshfree sub-domains, that is, $\Omega=\Omega_{FEM}\cup\Omega_{meshfree}$. The FE sub-domains consist of non-overlapping and conforming elements. The meshfree sub-domains are discretized into sets of points attached by weight functions with compact supports.

In the coupled model, the finite element approximation remains in the finite element sub-domains. The meshfree approximation is constructed in the meshfree sub-domains such that the continuity of the approximation remains across the interface between the finite element and mesh-free sub-domains or across the interface between any two mesh-free sub-domains. The function $\mathrm{u}(\mathbf{x})$ with $\mathbf{x}\in\Omega$ and $\Omega=\Omega_{FEM}\cup\Omega_{meshfree}$ is approximated by

$$\mathbf{u}^h(\mathbf{x}) = \begin{cases} \sum_{\substack{L=1 \\ \mathbf{x}_L \in \Omega_{FEM}}}^{KP} \Phi_L^{[m]}(\mathbf{x})\mathbf{d}_L; & \forall \mathbf{x} \in \Omega_{FEM} \\ \sum_{\substack{I=1 \\ \mathbf{x}_I \in \Omega_{meshfree}}}^{NP} \Psi_I^{[n]}(\mathbf{x}; \mathbf{x}-\mathbf{x}_I)\left[\mathbf{d}_I - \sum_{\substack{J=1 \\ \mathbf{x}_L \in \Gamma_{Interface}}}^{MP} \Phi_J^{[m]}(\mathbf{x}_I)\mathbf{d}_J\right] & \\ \quad + \sum_{\substack{L=1 \\ \mathbf{x}_L \in \Gamma_{Interface}}}^{MP} \Phi_L^{[m]}(\mathbf{x})\mathbf{d}_L = \sum_{\substack{I=1 \\ \mathbf{x}_I \in \Omega_{meshfree}}}^{NP} \hat{\Psi}_I^{[n]}(\mathbf{x})\mathbf{d}_I; & \forall \mathbf{x} \in \Omega_{meshfree} \end{cases} \tag{7}$$

In Eq. (7), $\Phi_L^{[m]}$ is the regular *m*th-order finite element shape function and *KP* is the total number of nodes per element. Also, the interfaces between the finite element and mesh-free sub-domains are defined by $\Gamma_{Interface} = \Omega_{FEM} \cap \Omega_{meshfree}$. NP denotes the total number of meshfree nodes whose supports cover evaluation point $\mathbf{x}$, and *MP* is the total number of the finite element nodes which are on the interface and whose supports cover evaluation point $\mathbf{x}$. $\hat{\Psi}_I (I = 1, 2, \ldots, n)$ are the coupled finite element and mesh-free shape functions. When the finite element interpolation order [*m*] is equal to the reproducing order [*n*], it can be proved (Wang *et al*. 2009) that

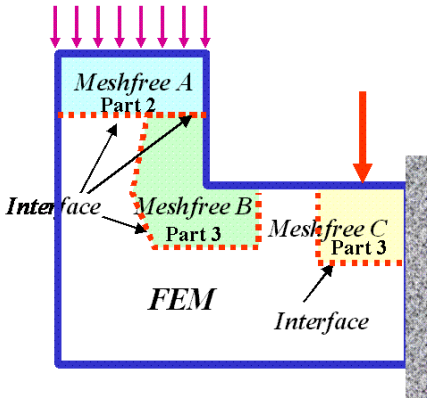

Fig.3Example of a coupled meshfree/finite element model

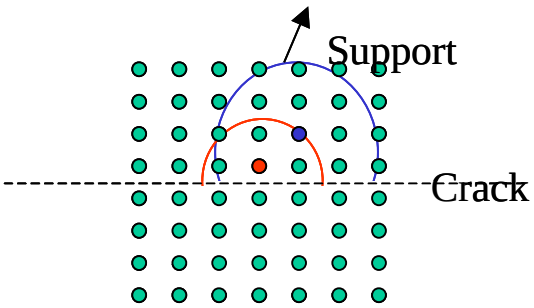

Fig.4 Visibility criterion in a crack

$$\hat{\Psi}_I(\mathbf{x}) = 0 \text{ for all nodes } \left\{ I : \text{support}(\Psi_I) \cap \Gamma_{Interface} \neq 0 \right\} \text{ and } \mathbf{x} \in \Gamma_{Interface} \tag{8}$$

Eq. (8) is called the *interface constraint*, i.e., the MLS shape function of all internal nodes becomes zero evaluated at the interface. If the *interface constraint* is satisfied, the resulting solution approximation of Eq. (7) becomes

$$u_i^h(\mathbf{x}) = \sum_{\substack{J=1 \\ \mathbf{x}_J \in \Gamma_{Interface}}}^{MP} \Phi_J^{[m]}(\mathbf{x}) d_{iJ}, \forall \mathbf{x} \in \Gamma_{Interface}. \tag{9}$$

In other words, the shape functions on the interface are reduced to the standard finite element shape functions and possess the Kronecker-delta property. Therefore, there are no conforming problems for the shape functions across the interface. In this study, bilinear finite elements are considered and a reproducing order of one is imposed on the meshfree approximation. Please refer to Wang *et al*. (2009) for detailed formulations on the coupled method.

3.Moving bundaryalgorithm and is numerical Implementation

In this section, the moving boundary algorithm for the meshfree method is presented to address the strong discontinuity and material separation issues in this study. These features are of great importance to the effective and accurate simulation of the self-piercing riveting process. The algorithm includes: (a) the inclusion of discontinuous shape functions to allow the material separation; (b) the introduction of moving boundaries to define the cracks and new contact surfaces. The moving boundaries also provide the visibility criterion for discontinuous approximation.

Belytschko*et al*. (Fleming *et al.* 1997, Krongauz and Belytschko 1998) described a method for construction of approximations around the tip of a discontinuity called the diffraction method. The method was motivated by the way light diffracting around a sharp corner, though the equations used in constructing the domain of influence and the weight function born almost no relationship to the equations of diffraction. This method was applied to the brittle materials under small strain assumption.Fig. 4 illustrates the basic concept of this approach where the discontinuity was introduced along the crack line through the visibility criterion near a crack.

When the crack moves in a ductile material, it can emit dislocations and stop propagation. The crack becomes blunted and begins to cause intense local deformation before next crack propagation. Under such circumstances, continuum damage mechanics offers advantages to predict the initiation and propagation of the cracks.

In this work, the continuum damage mechanics theory is adopted to define the failure of the material. The diffraction method based on the continuum damage mechanics is used to determine the discontinuous shape functions and to allow for a material separation. The evolution equationfor the damage variable is defined as

$$\dot{d} = \begin{cases} 0 & for \quad r \le r_d \\ \dfrac{Y}{S(1-d)}\dot{r} & for \quad r > r_d \end{cases} \tag{10}$$

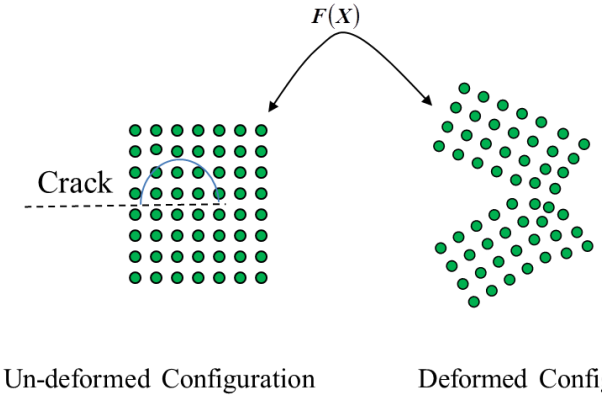

Fig. 5 Geometrical mapping in the meshfree computation domain subject to visibility criterion

where *d* is the damage variable, and *S* is the so-called strain energy release rate. The damage value *d=0* corresponds to the undamaged state, *d=dcritical*defines a complete local rupture. Damage can only develop for tensile stresses, and damage unloading is assumed to be an elastic process. r_d is the damage threshold. The material softening begins when the damage effective plastic strain reaches this value.*r* is the damage accumulated plastic strain or can be considered as the current damage threshold, and is calculated by

$$\dot{r} = \dot{\varepsilon}_{eff}^{p}(1-d) \tag{11}$$

where $\dot{\varepsilon}_{eff}^{p}$ is the effective plastic strain rate.

The term *Y*/*S*(1–*d*) shown in the damage evolution equation is an evolution function used to define the damage growth. This is similar to the hardening function used to define the hardening behavior in the plasticity model. *Y* is the elastic-damage potential energy, and is defined by

$$Y = \frac{1}{2}(1-d)\boldsymbol{e}_e : \boldsymbol{C}^0 : \boldsymbol{e}_e \tag{12}$$

Where$\boldsymbol{e}_e$is the elastic strain tensor, and $\boldsymbol{C}^0$is the virgin linear elasticity stiffness. The colon (**:**) signifies tensor contraction. This elastic-damage potential energy *Y* also characterizes the progressive degradation of mechanical properties of the material due to damage by means of a simple isotropic damage mechanism. A default of $\sigma_0/200$ is used in LS-DYNA where σ_0 is theinitial yield stress. The definition of variables can also be found in (LSTC 2012).

Since the material failure evolves in the large deformation region, it is advantageous to define the visibility criterion based on the un-deformed configuration as shown in Fig. 5. Because the spatial coordinates **x** and material coordinates**X** are one-to-one mapping between each other, the derivatives of material basis functions with respect to spatial coordinates can be carried out by chain rule to yield

$$\psi_{I,i} = \frac{\partial \psi_I(\mathbf{X}(\mathbf{x}))}{\partial \mathrm{x}_i} = \frac{\partial \psi_I(\mathbf{X}(\mathbf{x}))}{\partial \mathrm{X}_j}\frac{\partial \mathrm{X}_j}{\partial \mathrm{x}_i} = \frac{\partial \psi_I(\mathbf{X}(\mathbf{x}))}{\partial \mathrm{X}_j}F_{ji}^{-1} \tag{13}$$

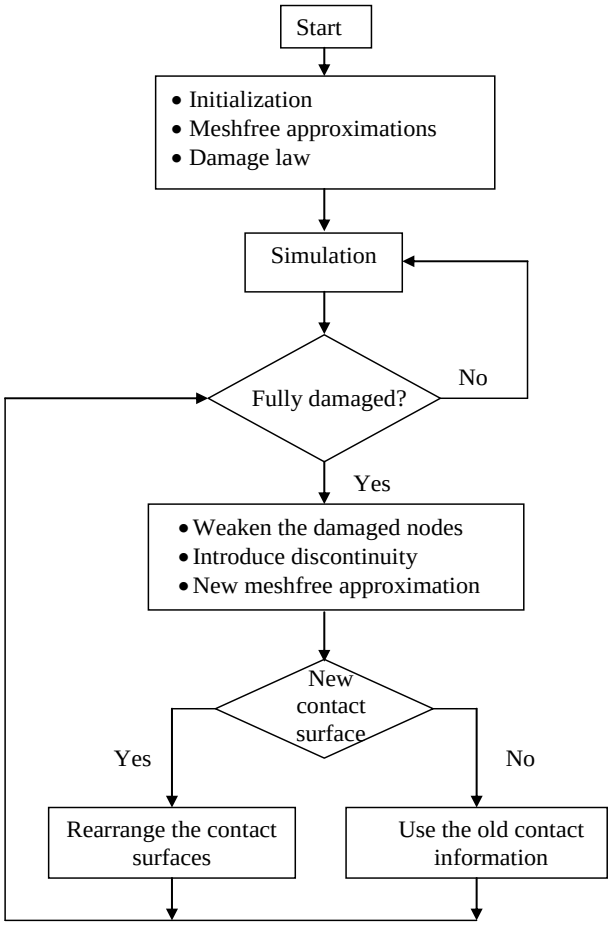

Fig 6 Flowchart for moving boundary method

Accordingly, the volume integrals in the assembly of discrete equations are computed in the un-deformed configuration as

$$\int_{\Omega_x} (\,)d\mathbf{x} = \int_{\Omega_X} (\,)\det|\boldsymbol{F}|d\mathbf{X} \tag{14}$$

When the material is completely damaged at a material point, the material loses its strength locally, and the associated nodes of that material point also lose contact and a new material interface forms. At this moment, the discontinuous meshfree shape functions are constructed based on the visibility criterion imposed on the new material interface defined in the un-deformed configuration. The overall moving boundary algorithm is described in Fig. 6.

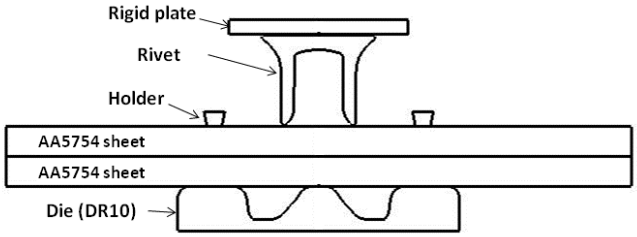

Fig.7 An assembly sketch of the SPR process in simulation

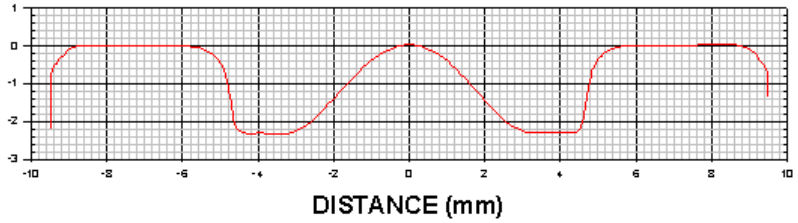

Fig.8 The geometry of the lower die (DR10 in Fig. 7)

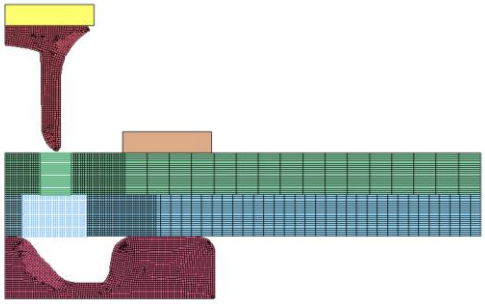

Fig.9 Discretization of the coupled meshfree/finite element SRP model (axi-symmetric)

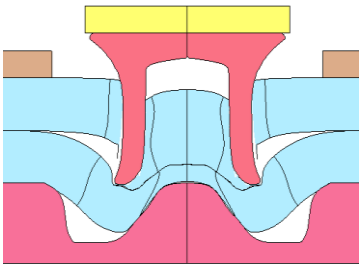

Fig.10 (a) Calculated deformation of the joint cross section when the rivet moves 5 mm into the sheets

Table 1 The material properties of the two aluminum plates are: Young's modulus E=70 GPa, Poisson's ratioρ=0.33 and piecewise linear plasticity as defined in Table 2

Yield stress (MPa)	Plastic strain
1340.0	0.00
1713.0	0.15

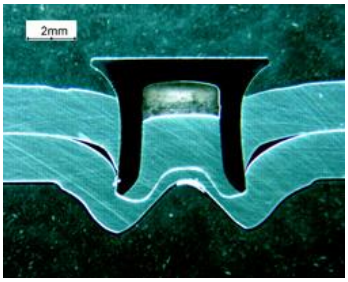

Fig.10 (b) Calculated deformation of the joint cross section when the rivet moves 5 mm into the sheets

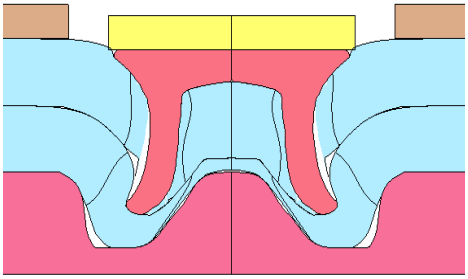

Fig.11 (a) Deformation of the joint cross section when the rivet moves 7 mm into the sheets (final stage)

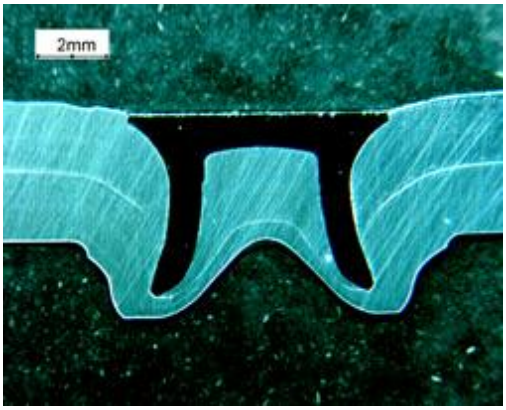

Fig.11(b) Deformation of the joint cross section when the rivet moves 7 mm into the sheets (final stage)

The deformation obtained by the present method at 5mm depth is illustrated in Fig. 10(a). The deformed shape obtained from the present method agrees quite well with the experimental data as shown in Fig. 10(b). Results also show that the proposed method successfully captures the material separation behavior near the piercing areas.

Finally, an effective plastic strain plot is presented in Fig. 12. A large plastic strain is observed near the rivet indicating the existence of large tension-shear mode, which is the dominant mechanism that causes the material failure.

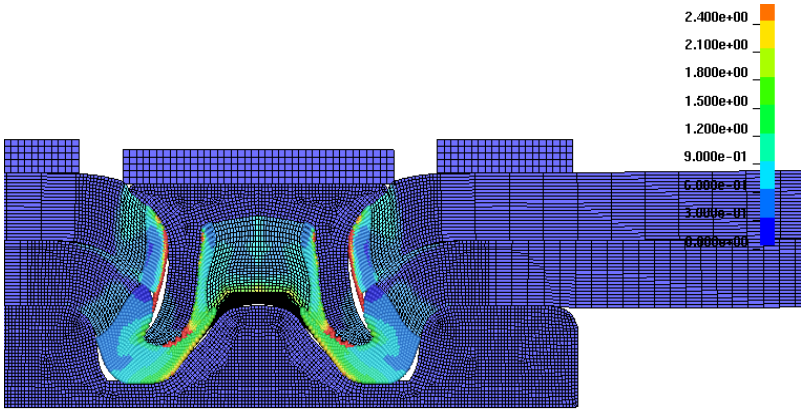

Fig. 12 Effective plastic strain plot shown in the joint cross section (final stage)

Table 2The material properties of the steel rivet are: Young's modulus E=210 GPa, Poisson's ratio ρ=0.31 and piecewise linear plasticity as defined in Table 1

Yield stress (MPa)	Plastic strain
150.0	0.00
195.0	0.15

Table 3The continuum damage mechanics model as described in Section 3 was employed for the modeling of material failure during the piercing process. The material constants relating to damage mechanics model as defined by LS-DYNA keyword *MAT_DAMAGE_1 (material type 104) are given in Table 3

Isotropic hardening parameterQ1 , C1 (MPa)	Damage threshold r_d	Rupture *dcritical*
1200, 0.2	0.2	0.8

4. The SPR process simulation

In this section, the accuracy of the present method is examined by comparing the numerical simulation with an experimental result. The SPR problem consists of two circular aluminum (AA5754) plates under clamped conditions and pierced by a steel rivet pushed down by a rigid plate at a speed of 20mm/s as shown in Fig. 7. Both the holder and the die are modeled as rigid bodies. The thickness of either aluminum plate is 2mm. Fig. 8 depicts the geometry of lower die which is fixed on the bottom. Fig. 9 is the corresponding numerical discretization of the problem using the axisymmetric model. As shown in Fig. 9, each plate is pre-divided into two areas, modeled by the mesh-free method (for the piercing area) and the finite element method (the remaining area), for the purpose of numerical efficiency. The mesh-free zones in two plates are chosen in a way such that they contain all the high gradients in the piercing process. The normalized support size is taken to be 1.2 in the mesh-free computation. Relatively dense discretization is used around the piercing areas in order to capture high stresses/strains and cracks. The frictional contact condition is considered between the rivet and aluminum plates with a coefficient of frictionμ = 0.15. The contact between two aluminum plates and die is assumed to be frictionless.

5. Conclusions

This paper presents a numerical technique for modeling large deformation and material separation phenomena in the SPR process. The coupled meshfree/finite element analysis method is adopted in this paper for an efficient meshfree simulation as well as to handle large material deformation involved in the material piercing. To consider the material failure in piercing process, a continuum damage mechanics is utilized in this study. A moving boundary algorithm based on the visibility criterion and un-deformed configuration is introduced into the meshfree approximation to numerically model the material separation in the ductile material. The numerical results are compared with the experimental data. The results have shown that the coupled meshfree/finite element model is able to deliver a numerically efficient and stable solution in dealing with large deformation. The moving boundary algorithm is also effective in modeling the material separation during the piercing process. From the study, it can be concluded that the present method provides a robust tool for simulating problems involving excessive material distortion and separation such as the SPR processes.

References

Babuska, I., Ihlenburg, F., Paik, E. and Sauter, S. (1995), "A generalized finite element method for solving the Helmholtz equation in two dimensions with minimal pollution", *Comput.Meth. Appl. M.*, **128**(3-4), 325-359.

Baiges, J. and Codina, R. (2013), "A variationalmultiscale method with subscales on the element boundaries for the Helmholtz equation", *Int. J. Numer.Meth. Eng.*,**93**(6), 664-684.

Belytschko, T. and Mullen, R. (1978), *On dispersive properties of finite element solutions*, Modern Problems in Elastic Wave Propagation, John Wiley & Sons, Ltd.

Belytschko, T., Lu, Y.Y. and Gu, L. (1994), "Element-free galerkin methods", *Int. J. Numer. Meth. Eng.*,**37**(2), 229-256.

Bouillard, P. and Suleau, S. (1998), "Element-free galerkin solutions for helmholtz problems: formulation and numerical assessment of pollution effect", *Comput. Meth. Appl. Mech. Eng.*, **161**, 317-335.

Franca, L.P., Madureira, A.L. and Valentin, F. (2005), "Towards multiscale functions: enriching finite element spaces with local but not bubble-like functions", *Comput. Meth.Appl. Mech. Eng.*, **194**(27-29), 3006-3021.

Farhat, C., Harari, I. and Franca, L.P. (2001), "The discontinuous enrichment method", *Comput.Meth. Appl. Mech. Eng.*, **190**, 6455-6479.

Harari, I. and Hughes, T.J.R. (1991), "Finite element method for the Helmholtz equation in an exterior domain: Model problems", *Comput. Meth. Appl. Mech. Eng.*, **87**(1), 59-96.

Harari, I. and Hughes, T.J.R. (1992), "Galerkin/least squares finite element method for the reduced wave equation with non-reflecting boundary conditions", *Comput.Meth. Appl. Mech. Eng.*, **98**(3), 441-454.

Harari, I. and Gosteev, K. (2007), "Bubble-based stabilization for the helmholtz equation", *Int. J. Numer.Meth. Eng.*,**70**(10), 1241-1260.

Harari, I. (2008), "Multiscalefinite elements for acoustics: Continuous, discontinuous, and stabilized methods", *Int. J. Numer. Meth. Eng.*,**6**, 511-531.

Hu, W., Wu, C.T. and Koishi, M. (2012), "A displacement-based nonlinear finite element formulation using meshfree-enriched triangular elements for the two-dimensional large deformation analysis of elastomers", *Finite Elem. Anal.Des.*,**50**, 161-172.

Hughes, T.J.R., Scovazzi, G. and Franca, L.P. (2004), *Multiscale and Stabilized Methods*, Encyclopedia of Computational Mechanics, John Wiley & Sons, Ltd.

Hughes, T.J.R. and Sangalli, G. (2007), "Variationalmultiscale analysis: the fine-scale Green's function,

projection, optimization, localization, and the stabilized methods", *SIAM J. Numer. Anal*., **45**(2), 539-557.
Ihlenburg, F. and Babuska, I. (1995), "Finite element solution of the Helmholtz equation with high wave number Part I: The h-version of FEM", *Comput. Math. Appl*., **30**(9), 9-37.
Ihlenburg, F. and Babuska, I. (1997), "Finite element solution of the helmholtz equation with high wave number Part II: The h-p version of FEM", *SIAM J. Numer. Anal*., **34**(1), 315-358.
Lai, S.J., Wang, B.Z. and Duan, Y. (2010), "Solving helmholtz equation by meshless radial basis functions method", *Prog. Electromagn. Res. B*, **24**, 351-367.
Liu, W.K., Jun, S. and Zhang, Y.F. (1995), "Reproducing kernel particle methods", *Int. J. Numer.Meth. Fl.*,**20**(8-9), 1081-1106.
Liu, W.K., Hao, W., Chen, Y., Jun, S. and Gosz, J. (1997), "Multiresolution reproducing kernel particle methods", *Comput. Mech*., **20**, 295-309.
Oberai, A.A. and Pinsky, P.M. (1998), "A multiscale finite element method for the helmholtz equation", *Comput.Meth. Appl. Mech. Eng.*, **154**(3-4), 281-297.
Oberai, A.A. and Pinsky, P.M. (2000), "A residual-based finite element method for the helmholtz equation", *Int. J. Numer.Meth. Eng.*,**49**(3), 399-419.
Park, C.K., Wu, C.T. and Kan, C.D. (2011), "On the analysis of dispersion property and stable time step in meshfree method using generalized meshfree approximation", *Finite Elem. Anal.Des*.,**47**(7), 683-697.
Suleau, S. and Bouillard, P. (2000), "One-dimensional dispersion analysis for the element-free Galerkin method for the Helmholtz equation", *Int. J. Numer.Meth. Eng.*,**47**(6), 1169-1188.
Uras, R.A., Chang, C.T., Chen, Y. and Liu, W.K. (1997), "Multi-resolution reproducing kernel particle methods in Acoustics", *J. Comput.Acoust.*,**5**, 71-94.
Voth, T.E. and Christon, M.A. (2001), "Discretization errors associated with reproducing kernel methods: one-dimensional domains", *Comput. Meth.Appl. Mech. Eng.*, **190**(18-19), 2429-2446.
Wenterodt, C. and von Estorff, O. (2009), "Dispersion analysis of the meshfree radial point interpolation method for the helmholtz equation", *Int. J. Numer.Meth. Eng.*,**77**(12), 1670-1689.
Wu, C.T. and Koishi, M. (2009), "A meshfree procedure for the microscopic analysis of particle-reinforced rubber compounds", *Interact. Multiscale Mech*., **2**(2), 129-151.
Wu, C.T., Park, C.K. and Chen, J.S. (2011), "A generalized approximation for the meshfree analysis of solids", *Int. J. Numer.Meth. Eng.*,**85**(6), 693-722.
Wu, C.T. and Hu, W. (2011), "Meshfree-enriched simplex elements with strain smoothing for the finite element analysis of compressible and nearly incompressible solids", *Comput.Meth.Appl. Mech. Eng.*, **200**(45-46), 2991-3010.
Wu, C.T., Hu, W. and Chen, J.S. (2012), "A meshfree-enriched finite element method for compressible and near-incompressible elasticity", *Int. J. Numer.Meth. Eng.*,**90**(7), 882-914.
Wu, C.T. and Koishi, M. (2012), "Three-dimensional meshfree-enriched finite element formulation for micromechanical hyperelastic modeling of particulate rubber composites", *Int. J. Numer.Meth. Eng.*,**91**(11), 1137-1157.
Wu, C.T., Guo, Y. and Askari, E. (2013), "Numerical modeling of composite solids using an immersed meshfreeGalerkin method", *Composit. B*, **45**(1), 1397-1413.
Yao, L.Y., Yu, D.J., Cui, X.Y. and Zang, X.G. (2010), "Numerical treatment of acoustic problems with the smoothed finite element method", *Appl. Acoust.*, **71**(8), 743-753.
You, Y., Chen, J.S. and Voth, T.E. (2002), "Characteristics of semi- and full discretization of stabilized Galerkinmeshfree method", *Finite Elem. Anal.Des*.,**38**(10), 999-1012.